small methods
www.small-methods.com

Photonic Interfaces: an Innovative Wearable Sensing Solution for Continuous Monitoring of Human Motion and Physiological Signals

Yingchun Wu, Kangjian Bao, Junxuan Liang, Zongxi Li, Yilin Shi, Renjie Tang, Kai Xu, Maoliang Wei, Zequn Chen, Jialing Jian, Ye Luo, Yiheng Tang, Qingyan Deng, Hao Dai, Chunlei Sun, Wei Zhang, Hongtao Lin, Kewei Zhang, and Lan Li**

Flexible integrated photonic sensors are gaining prominence in intelligent wearable sensing due to their compact size, exceptional sensitivity, rapid response, robust immunity to electromagnetic interference, and the capability to enable parallel sensing through optical multiplexing. However, integrating these sensors for practical applications, such as monitoring human motions and physiological activities together, remains a significant challenge. Herein, it is presented an innovative fully packaged integrated photonic wearable sensor, which features a delicately designed flexible necklace-shaped microring resonator (MRR), along with a pair of grating couplers (GCs) coupled to a fiber array (FA). The necklace-shaped MRR is engineered to minimize waveguide sidewall-induced scattering loss, with a measured intrinsic quality factor (Q_{int}) of 1.68×10^5, ensuring highly sensitive and precise signal monitoring. GCs and FA enhance the seamless wearability of devices while maintaining superior sensitivity to monitor various human motions and physiological signs. These are further classified signals using machine learning algorithms, achieving an accuracy rate of 97%. This integrated photonic wearable sensor shows promise for human-machine interfaces, touch-responsive wearable monitors, and artificial skin, especially in environments susceptible to electromagnetic interference, such as intensive care units (ICUs) and spacecraft. This work significantly advances the field of smart wearable technology.

1. Introduction

The advancements in fields such as robotics, prosthetics, and human-machine interfaces have created a significant demand for wearable sensors. These sensors are essential for accurately monitoring human motions and physiological activities, capturing the nuanced dynamics of human movements, muscle activities, and other physiological signals. Consequently, this demand dictates exacting specifications for wearable sensors, encompassing low power consumption, high adaptability to body contours, exceptional accuracy, minimal signal interference, and the provision for real-time data acquisition.[1] Advancements in wearable sensor technologies are categorized into flexible electronic and photonic technologies. The former has made remarkable progress in the real-time monitoring of various human motions[2] and physiological activities.[3] For instance, it has been successfully applied to monitor physiological parameters such as wrist pulse,[4]

Y. Wu
Zhejiang University
Hangzhou 310058, China

Y. Wu, K. Bao, Z. Li, Y. Shi, R. Tang, Z. Chen, J. Jian, Y. Luo, Y. Tang, Q. Deng, C. Sun, L. Li
Zhejiang Key Laboratory of 3D Micro/Nano Fabrication and Characterization
Department of Electronic and Information Engineering
School of Engineering
Westlake University
Hangzhou 310030, China
E-mail: lilan@westlake.edu.cn

Y. Wu, K. Bao, Z. Li, Y. Shi, R. Tang, Z. Chen, J. Jian, Y. Luo, Y. Tang, Q. Deng, C. Sun, L. Li
Institute of Advanced Technology
Westlake Institute for Advanced Study
Hangzhou 310024, China

J. Liang, K. Zhang
State Key Laboratory of Bio-Fibers and Eco-Textiles
College of Materials Science and Engineering
Qingdao University
Qingdao 266071, China
E-mail: zhkw@qdu.edu.cn

K. Xu, M. Wei, H. Dai, H. Lin
MOE Frontier Science Center for Brain Science & Brain-Machine Integration
Key Laboratory of Micro-Nano Electronics and Smart System of Zhejiang Province
College of Information Science and Electronic Engineering
Zhejiang University
Hangzhou, Zhejiang 310027, China

The ORCID identification number(s) for the author(s) of this article can be found under https://doi.org/10.1002/smtd.202500727

DOI: 10.1002/smtd.202500727

heartbeat,[5] respiration,[6,7] blood pressure,[8] glucose levels,[9] cholesterol levels,[10] blood oxygen concentration,[2] metabolites,[11] perspiration[12] and to detect human motions.[7,13] Flexible electronics[4,12,14–20] have enabled unprecedented applications for wearable devices and accelerated advancements in flexible photonics. Flexible photonics technology offers higher bandwidth and data transmission rates compared to electronic technology. Furthermore, optical signals are inherently immune to electromagnetic interference. This characteristic enables flexible photonic devices to maintain stable operation in sensitive electromagnetic environments, such as those found in medical equipment and space technology. Specifically, photonic technology in the medical field can be utilized for non-invasive and precise stimulation in the treatment of neurological disorders.[21–23]

In wearable photonics, fiber optic sensors[24] represent a quintessential example enabled by high sensitivity to temperature,[25,26] pressure,[25,26] strain,[27,28] and other physical signals.[29–32] Optical micro/nano fibers,[26,27,29] hydrogel optical fibers,[33,34] PDMS optical fibers,[33,35,36] thermoplastic elastomer optical fibers,[37] PLGA fiber,[25] and PDMS-embedded silica microfibers,[30,38] have been developed into wearable devices. These technologies face constraints in integration, large-scale manufacturing, and spatial degree of freedom. Flexible integrated photonics devices retain the advantages of optical fiber sensors to overcome the aforementioned challenges. They enable multifunctional unit integration[39,40] at micrometer scales, combining CMOS-compatible fabrication and universal manufacturing technology[41] for low-cost mass production. This approach supports 2D conformal designs through flexible arrangement of sensing components,[42] while maintaining compatibility with on-chip light sources/detectors.[43–45] This capability enables advanced applications like the detection of biological processes at subcellular levels,[18] smart photonic skin development,[46] precision drug delivery,[47] and high-speed medical imaging.[48] Recent developments have included flexible silicon photonics,[49] single-mode stretchable photonic waveguides,[50] bendable[51] and stretchable integrated photonics sensors.[50] However, these sensors currently lack prototypes for direct human-skin wearable applications.

Herein, we propose an innovative fully packaged wearable integrated photonics sensing solution (**Figure** 1a) that achieves high-sensitivity, plug-and-play functionality, and machine learning-assisted classification for various signals. Our optimized necklace-shaped microring resonator (MRR) sensor demonstrates a high intrinsic Q (Q_{int}) factor (1.6×10^5), enabling highly sensitive real-time monitoring of human motion and physiological signals. A fiber array (FA) integrated with a grating coupler (GC) was utilized to achieve the plug-and-play functionality. The plug-and-play functionality enhances the system's wearability while maintaining superior sensitivity. Our sensing solution incorporates artificial neural networks (ANNs) for classifying subtle signal characteristics, enabling 97% accurate differentiation of 15 specific human signals. The integration of the wearable integrated photonic sensor with an ANN demonstrates a new multifunctional, intelligent wearable device.

2. Results and Discussion

2.1. Design and Fabrication of Wearable Integrated Photonic Sensor

2.1.1. Design a Fully-Packaged Wearable Integrated Photonic Sensor

The schematic illustration and photographs of the fully packaged wearable integrated photonic sensing solution based on the necklace-shaped MRR are shown in Figure 1b,c. MRRs are circular waveguides that support standing wave modes, where light signals propagate back and forth around the ring. When the resonance condition is met, light from the bus waveguide couples into the MRR, and the lightwave's round trip in the ring is in phase with the incoming lightwave, resulting in periodic resonant peaks in the transmission spectrum. Changes in the MRR's cross-sectional area and length can lead to resonance peak shifts due to the modification in the effective refractive index. These shifts are mainly due to minor stress or strain. External forces induce slight geometrical changes in the MRR, affecting the light's optical path and phase and causing resonance peak drift, resulting in a linear strain-optical coupling relationship.[51,52] The sensing property detects subtle stress/strain changes from environmental variations, with resonance peak shifts indicating wavelength-specific optical transmission power changes, as depicted in Figure 1d. After measuring the resonance peak of the unstrained microring, we monitor the temporal variations in the light intensity at the wavelength corresponding to the resonance peak. Our sensing mechanism utilizes this principle to enable precise mapping of human movements and physiological characteristics (Figure 1e).

The sensor unit is fabricated on ChG material $Ge_{28}Sb_{12}Se_{60}$ (GSSe) core layer (300 nm thick), sandwiched between two SU-8 cladding layers (1.4 µm thick each), and supported by a commercial polyimide (PI) film tape substrate. A fiber array (FA) integrated with a grating coupler (GC) was used to assemble a packaged sensor, as displayed in Figure 1c. The refractive indices of GSSe (2.68) and SU-8 (1.58) at 1550 nm ensure strong light confinement. A necklace-shaped MRR with a 20 µm radius (Figure 1b,c) optimizes sensitivity through strain-induced resonance shifts, while the PI substrate ensures mechanical flexibility for conformal wearability in various applications (Figure 1e).This design supports real-time monitoring of physiological and motion signals and can be enhanced ANN for signal classification, as displayed in Figure 1f. Scalability is achieved through the dense integration of multiple sensing units in compact spatial ranges,[42] facilitating 2D conformal sensing for wearable applications such as smart skin,[18,46,53] which addresses fiber optic's limitations.

Optimal device morphology and dimensions were determined through theoretical calculations and simulations. Our design

---

W. Zhang
Zhejiang Key Laboratory of Advanced Optical Functional Materials and Devices
Faculty of Electrical Engineering and Computer Science
Ningbo University
Ningbo 315211, China

L. Li
Westlake Institute for Optoelectronics
Hangzhou 311421, China

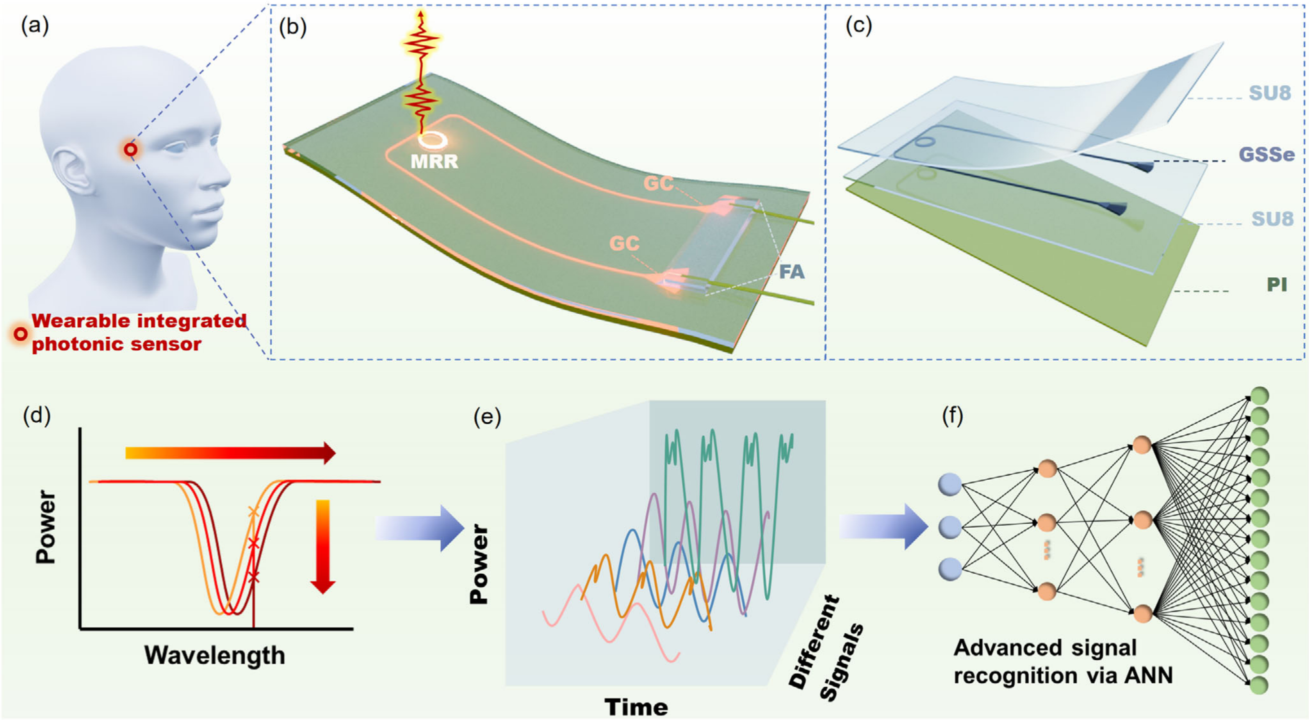

Figure 1. Design architecture and working principle of the wearable integrated photonic sensor for monitoring human motion and physiological signals. a) Illustration of the wearable integrated photonic sensor for motion and physiological monitoring. b) Schematic of a packaged wearable integrated photonic sensor. c) Exploded view of the photonic sensor architecture with multiple layers of different materials. d) The working mechanism of the photonic sensor, accompanied by resonance peak drift in the MRR's transmission spectrum due to applied microscopic stress or strain. e) Continuous monitoring of the temporal variations of the transmitted optical power at the resonance peak induced by modulation signals. f) Data workflow: preprocessing → machine learning → ANN classification.

features a necklace-shaped MRR (**Figure** 2a) optimized for high Q factors by minimizing waveguide loss α through structural optimization.[54] The MRR configuration comprises an upper multimode half-ring characterized by an outer radius of R_{out} and an inner radius of R_{min}, as well as a lower half ring with an outer radius of R_{out} and an inner radius gradient with a bending angle from R_{max} to R_{min} (Figure 2a). Structural parameters optimization yielded $R_{out} = 20$ µm, $R_{max} = 19.3$ µm, and $R_{min} = 18.3$ µm. The optimization process and results are thoroughly discussed in supplementary Figure S1 (Supporting Information). Notably, the bottom part of the MRR is ingeniously devised as a waveguide gradient, facilitating a seamless transition from a single-mode region to a multimode region to ensure the efficient coupling of fundamental modes while suppressing the excitation of higher-order modes. Figure 2b depicts the simulated light propagation field in the 90°bending width-gradient waveguide from 700 nm (input) to 1700 nm (output). The related mode profiles are shown in Figure 2c. The material parameters used in the simulation are consistent with reality, featuring a 300 nm-thick GSSe core and an ≈1.4 µm-thick SU-8 cladding. Almost no multimode interference is observed, indicating the effectiveness of the designed 90 ° bending width-gradient waveguide. Here, the scattering loss induced by sidewall roughness in the optical waveguide is calculated using the equation:[55]

$$\alpha = \frac{\sigma^2}{\sqrt{2}k_0 d n_1} g\left(n_1, n_2\right) f_e\left(n_1, n_2, L_c\right) \tag{1}$$

where σ is the waveguide sidewall roughness; k_0 is the wavenumber in vacuum; d is half of the waveguide width; n_1,n_2 are the refractive index of the waveguide core and the cladding layer, respectively; L_c is the correlation length; $g(n_1,n_2)$ is the waveguide geometry factor and $f_e(n_1,n_2,L_c)$ is the spectral density factor. Thus, a $\sigma - Loss$ relation (assuming $L_c = 20$ nm, operation wavelength at 1500 nm) is obtained in Figure 2d, the sidewall roughness induced loss of the fundamental mode at output port (waveguide width = 1700 nm, bending radius = 19.15 µm) is much lower than that of the fundamental mode at input port (waveguide width = 700 nm, bending radius = 19.65 µm) under the same σ while high-order modes induce more loss than that the fundamental mode does over the same waveguide width and bending radius. Therefore, the design prioritizes strong high-order mode suppression, with the width-gradient bent waveguide demonstrating ≈50 dB suppression across 1400–1600 nm (Figure 2e).

2.1.2. Fabrication of a Fully-Packaged Wearable Integrated Photonic Sensor

As illustrated in Figure S2 (Supporting Information), the fabrication process started by coating and curing an SU-8 layer on a rigid wafer with a 500 nm-thick SiO_2 layer. The core sensing unit, a necklace-shaped MRR on a GSSe layer (Figure 2f), was then fabricated, along with a pair of GCs at the ends of the bus waveguide

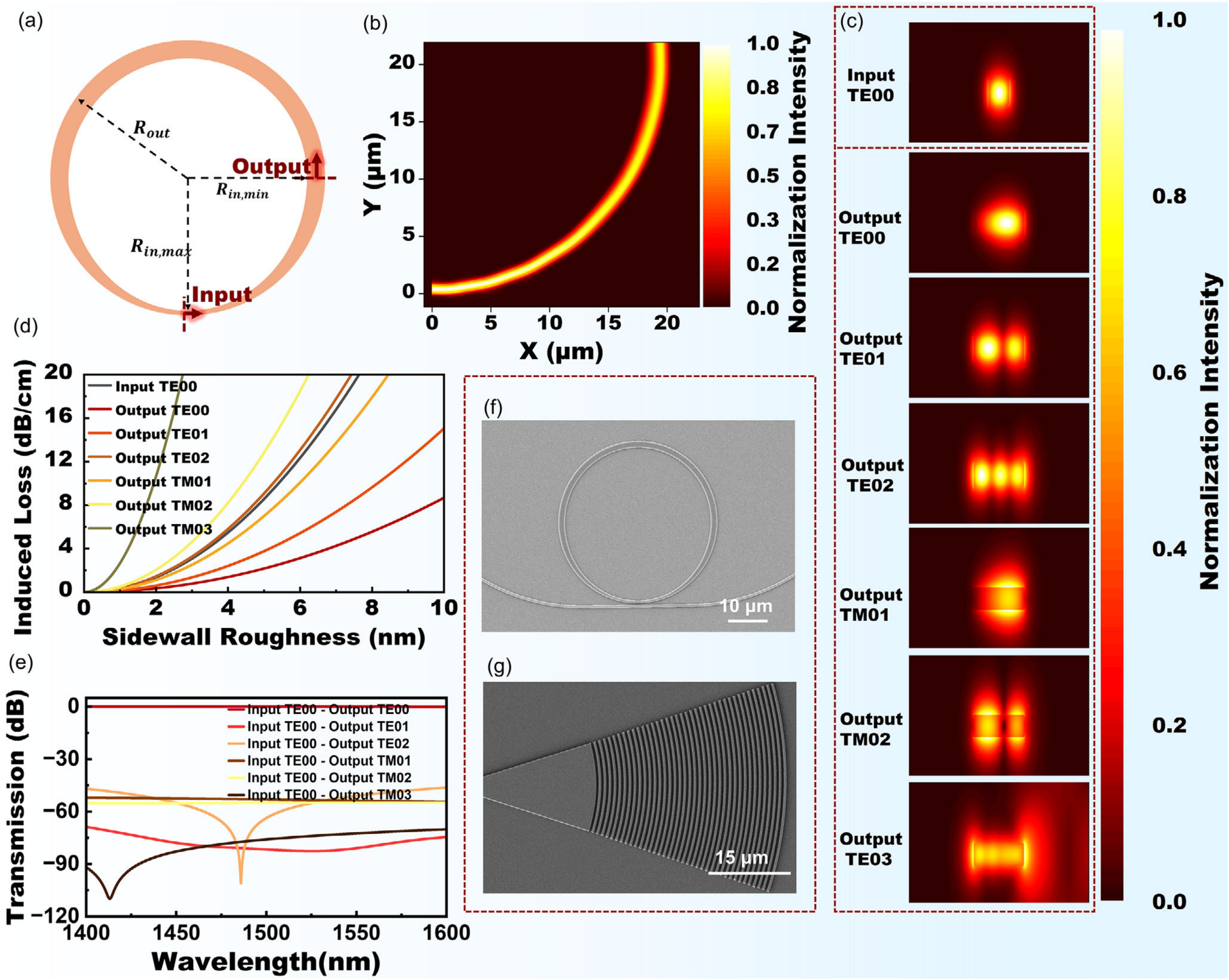

Figure 2. Design and performance characterization of the wearable integrated photonic sensor. a) Top-view morphology of the designed MRR. b) Simulated light propagation in the designed bending width-gradient waveguide. c) Mode profiles at the input and output ports. d) Calculated scattering loss/sidewall roughness relationship for different modes at the input and output sites. e) Calculated respective mode excitation ratios of the higher-order modes excited by TE0 mode in the 90° bending width-gradient waveguide. f) Scanning electron micrograph (SEM) of a necklace-shaped MRR sensor and a bus waveguide. g) SEM of a GC.

(Figure 2g). This coupling strategy played a crucial role in optimizing the sensitivity and accuracy of the sensing unit, making it suitable for various applications and facilitating reliable, long-time data collection and signal monitoring. To achieve a high-performance film, a 300 nm-thick GSSe film was deposited using the E-beam evaporation deposition method, and its thickness was characterized, as depicted in Figure S3a (Supporting Information). The optical properties, including refractive index and extinction coefficient, were identified using an ellipsometer (J.A. Woollam RC2 XI+) and presented in Figure S3b (Supporting Information). Patterning of MRR, bus waveguide, and a pair of GCs was accomplished through electron beam lithography (EBL Elinix 125 kV) on maN 2403 electron beam resist, followed by the transfer of the patterns onto the lower GSSe layer using inductively coupled plasma (ICP) techniques. The fabricated patterns are outlined in Figure 2f,g (SEMs), while Figure S4 (Supporting Information) (optical micrographs). The upper cladding layer was subsequently applied to form a robust and optically functional composite structure. Finally, the structure was carefully transferred from the rigid wafer onto a flexible substrate, a PI film tape. This transfer process ensured that the composite structure could maintain its integrity and functionality while adapting to the flexibility of the substrate. To enable flexible deployment of the sensing unit across diverse application scenarios, the flexible device was encapsulated with GCs and an FA with the help of a custom-built packaging system (Figure S5, Supporting Information), resulting in a packaged flexible integrated photonics sensor, which is visually presented in both physical (Figure S6 Supporting Information) and schematic (Figure 1a) representations.

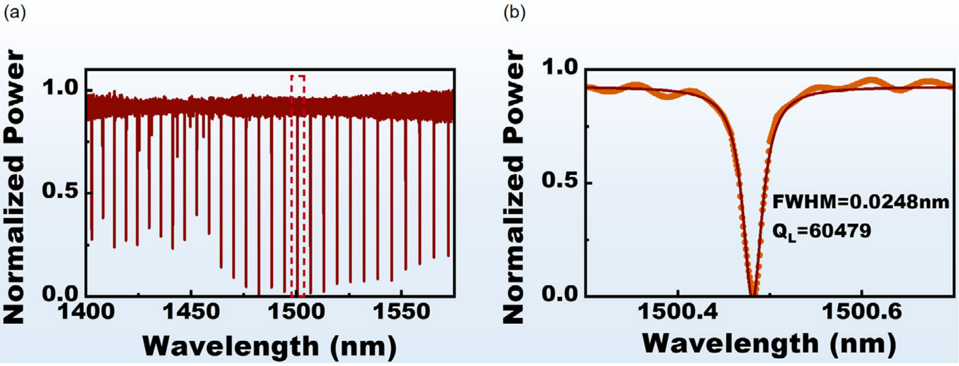

Figure 3. a) Normalized transmission spectrum of the necklace-shaped MRR sensor. b) Typical resonance with a full width at half maximum (FWHM) of 0.0248 nm.

2.2. Characterization of the Necklace-Shaped High-Q MRR Sensor

To demonstrate the real-time signal detection capability, the following procedure was employed: a comprehensive scan of the transmission spectrum of the necklace-shaped MRR is performed, and the wavelength point with the sharpest peak, selected for its high sensitivity, is identified, a narrow linewidth laser is precisely tuned to this wavelength point and input into the MRR, and the optical power output from the MRR is continuously monitored to detect and analyze real-time signal variations, effectively capturing and analyzing human motion and physiological signals in real-time. The setup includes a tunable laser with multi-wavelength scanning and single-wavelength output, a multi-channel power meter, and a data acquisition card (Figure S7, Supporting Information).

The operating principle of the MRR cavity sensor is based on the shift in resonant wavelength under varying external influences, such as microstress or microstrain. Accurate measurements require evaluating the resonance peak of the unstrained MRR without any external influences in advance. A typical transmission spectrum of the MRR sensor (**Figure 3**a), demonstrates fundamental mode resonances with an extinction ratio of over 10 dB within the wavelength range of 1450–1550 nm. Notably, a high Q factor of $\approx 4–6 \times 10^4$ (Q_L) is achieved, with a specific example of Q_L recorded as 60479 in the proximity of 1500 nm (Figure 3b), yielding an intrinsic Q (Q_{int}) of 1.68×10^5. The high Q-factor enables enhanced wearable sensing sensitivity through the MRR's sharp resonance peak, where minute external changes induce abrupt power intensity shifts.

2.3. Advanced Detection and Recognition of Human Motions and Physiological Signals

2.3.1. Human Motion and Physiological Signal Monitoring

The performance of the sensor was evaluated through human motion monitoring, hand gesture recognition, detailed head movement analysis, and the sensitive detection of minute muscle movements, targeting eyeball movement. All of the demonstration experiments were tested in an environmental factor-controlled condition. The influence of environmental factors such as temperature and humidity is excluded in Figure S8 (Supporting Information). As **Figure 4**a shows, the packaged flexible sensor was adhered to the wrist. Finger bending (other body parts in a static state) induced a meridian and micro-muscle movement on the wrist (Detailed process of the subtle movements of meridians and muscle groups caused by finger movements are captured in Figure S9, Supporting Information) and propagated to the sensor, stretching or compressing the MRR structure. This generates a significant resonant wavelength shift and an external bending loss, producing a distinct power output change (e.g., thumb bending: 2.7–3.4 dB upward pulse; index finger: 1.0–1.5 dB reverse pulse). Conversely, when the finger resumes its original position, the MRR reverses its response, reversing the power output shift relative to bending. (Figure 4a) Subsequently, the response of bending and resuming was investigated for each middle finger, ring finger, and little finger. Complex gestures like thumb double-bends, scissor motions, and fist formations generate distinct spectral signatures enabling precise gesture recognition (Figure 4). Furthermore, the power output responses of five individual finger actions (Figure 4a) were collectively compared to those of the three more complex finger movements. The obtained results have successfully demonstrated the sensor's capability to effectively discriminate and classify various gestures, exhibiting prompt response times. Notably, a single sensor suffices for multi-gesture classification without positional adjustments, making it more convenient and simpler to use without compromising its sensitivity, compared to a flexible electronics solution, which requires multiple sensors distributed on all the moving fingers.[3,56–60] Consecutively, demonstrations for both large-amplitude body movements and subtle muscle movements were conducted. For head movements, neck-mounted sensors detect raising (+20 dB), and nodding (−60 dB) through power changes. When participants raised their heads, nodded, or shook their heads from side to side (other body parts in a static state), our photonic sensor exhibited exceptional sensitivity, allowing us to easily identify different head movements accurately by analyzing the pulse waveform characteristics (Figure 4b) and monitor them in real time (Movie S1, Supporting Information). And brow ridge-mounted sensors track subtle eyeball movements through pressure-induced power variations, with unique time-power patterns for sleep quality assessment. The unique

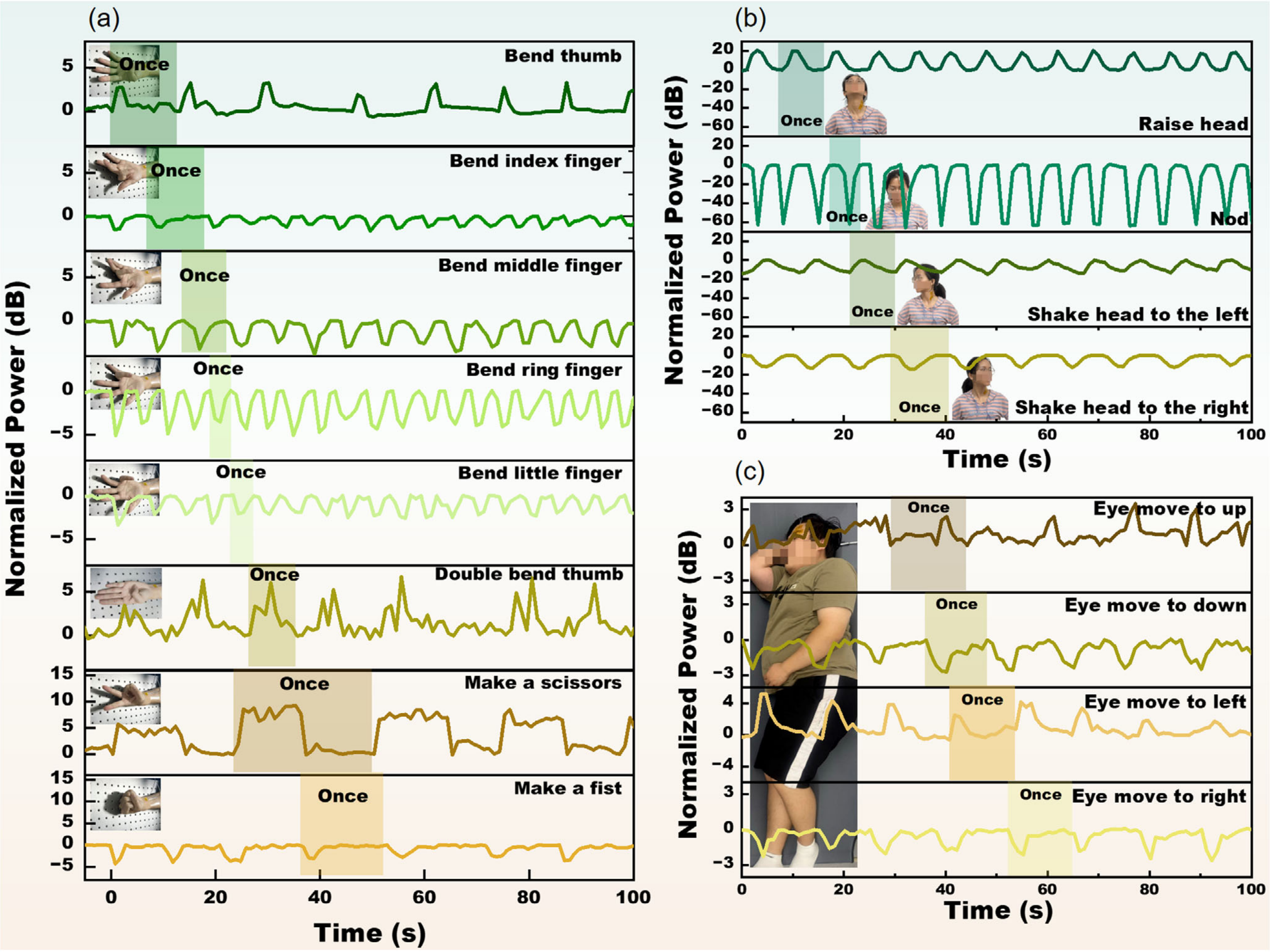

Figure 4. Dynamic power response of the packaged wearable integrated photonic sensor for human motions. a) Hand gesture recognition (8 types). b) Head movement monitoring (4 types). c) Eyeball movement monitoring during sleep.

patterns enabled us to perceive different directions for eyeball movement, as depicted in Figures 4c and S10 (Supporting Information). This capability underscores the sensor's effectiveness in providing detailed and reliable data for assessing sleep quality, ultimately contributing to better health monitoring and management. Therefore, the sensor demonstrates high sensitivity, versatility, and real-time capability in wearable health monitoring, supporting applications from gesture recognition to physiological signal tracking. And we confirm the reliability of our sensor in complex movement scenarios when simultaneous actions, as shown in Figure S11 (Supporting Information).

Furthermore, the packaged wearable integrated photonic sensor demonstrated versatility in monitoring diverse physiological activities, including blinking, deep breathing, swallowing, and neck pulse tracking (other body parts in a static state), when positioned on the temple, nose, throat, and neck (**Figure** 5a–e). The results, as depicted in Figure 5a–e, clearly demonstrate the distinctive characteristics of the continuous power response spectra associated with these physiological actions. For example, an upward sharp characteristic pulse appears on the spectrum image once the participant generates a blinking action (Movie S2, Supporting Information), enabling direct frequency extraction of physiological signals through pulse waveform counting and temporal analysis. These signals were effectively differentiated from body and gesture movements, highlighting the sensor's multimodal detection capability, as collectively illustrated in Figure 5e. By merging high sensitivity with multi-parameter tracking, this work highlights the potential of integrated photonics in real-time monitoring, wearable health devices, and human-computer interaction.

2.3.2. Advanced Signal Recognition via ANN-Based Machine Learning Algorithms

Given the multitude of human motions and physiological signals, accurate identification becomes challenging due to subtle differences between signals. To address this, machine learning algorithms were employed to achieve precise recognition. The power-time data is transformed into a series of features, including the width, height, mean, prominence, energy, area, rate of change, falling slope, and tend of the peak in the transmission

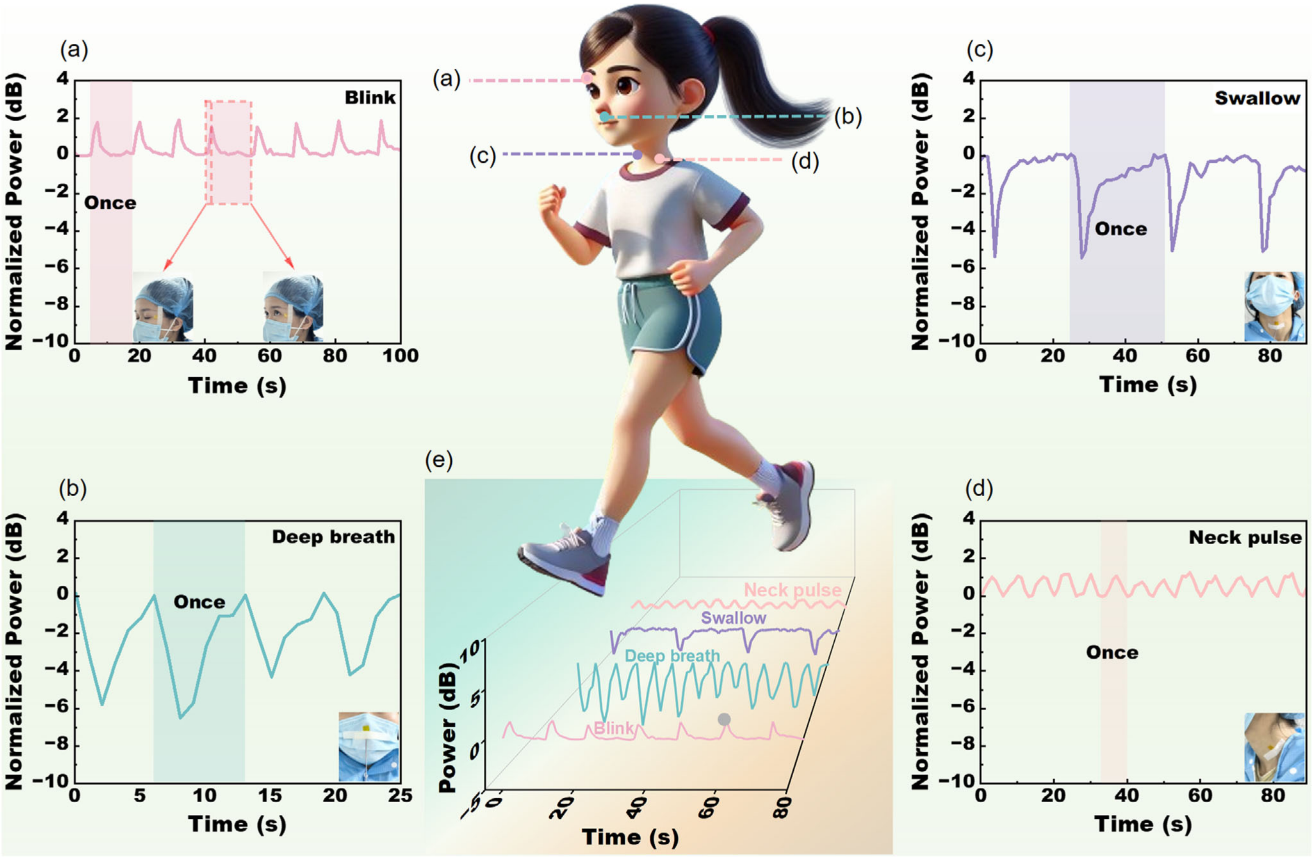

Figure 5. Dynamic power response of packaged wearable integrated photonic sensor for physiological activities. a) Eye blinking detection (temple). b) Deep breathing analysis (nose). c) Swallowing activity sensing (foreneck). d) Neck pulse monitoring (hindneck). e) Collective physiological signal responses (4 types).

spectra. Selecting the appropriate features to build the dataset is crucial before conducting the data training in the machine learning model. For the random forest law, the most important features, peak height, peak mean, and peak prominence, were chosen based on feature importance ranking results (**Figure** 6a). In the proof-of-the-concept demonstration, four head movements and four physiological movements, such as blinking, swallowing, neck pulse variation, and deep breathing are selected as the human feature signs. Each 2D dataset representing these power-time features was randomly divided into 150 sequences to cover the entire test data for each feature. Subsequently, the extracted features were trained through ANN with 32 and 64 neurons in each of the hidden layers (Figure 6b), and the accuracy of all states from both the training and validation data approached almost 100% after 100 epochs (Figure 6c), as evidenced by the accuracy and normalized loss for the two objective functions during 200 iterations (Figure 6d). The classified features align with the tested states, forming the confusion matrix (Figure 6e). The machine learning model achieved an overall prediction accuracy of 97% for the 15 states/features examined (Figure 6e), demonstrating the excellent performance of the ANN-based 2D-SFE for multidimensional vector prediction. To further validate the superior performance of the ANN-based algorithm for human signal recognition, various algorithms, including K-nearest neighbors (KNN), random forest (RF), logistic regression, support vector machine (SVM), gradient boosting, Naïve Bayes, and decision tree, were compared. The prediction accuracies were 86%, 93%, 86%, 44%, 86%, 80%, 95%, and 96% for ANN, respectively, as displayed in Figure 6f. Among these algorithms, the ANN model exhibited the most prominent performance, making it the optimal choice for this type of recognition task. To validate the consistency and reliability of our results, we doubled the sample size. The results, shown in Figure S12 (Supporting Information), demonstrate that the increase in the number of participants had minimal impact on the final prediction accuracy. Therefore, the application of machine learning algorithms based on the ANN enables highly accurate recognition and classification of signals obtained from our designed wearable integrated photonic devices. This approach extends the potential applications of wearable integrated photonic sensors in real-time health monitoring, personalized medicine, and advanced human-computer interaction.

3. Conclusion

In summary, the fully packaged wearable integrated photonic sensing solution demonstrates robust real-time monitoring of human motions or physiological activities, including finger and head gestures, blinking, breathing, swallowing, and neck pulse detection. Its novel design, necklace-shaped MRR achieves a high Q factor (1.68×10^5) for enhanced sensitivity. Its packaged

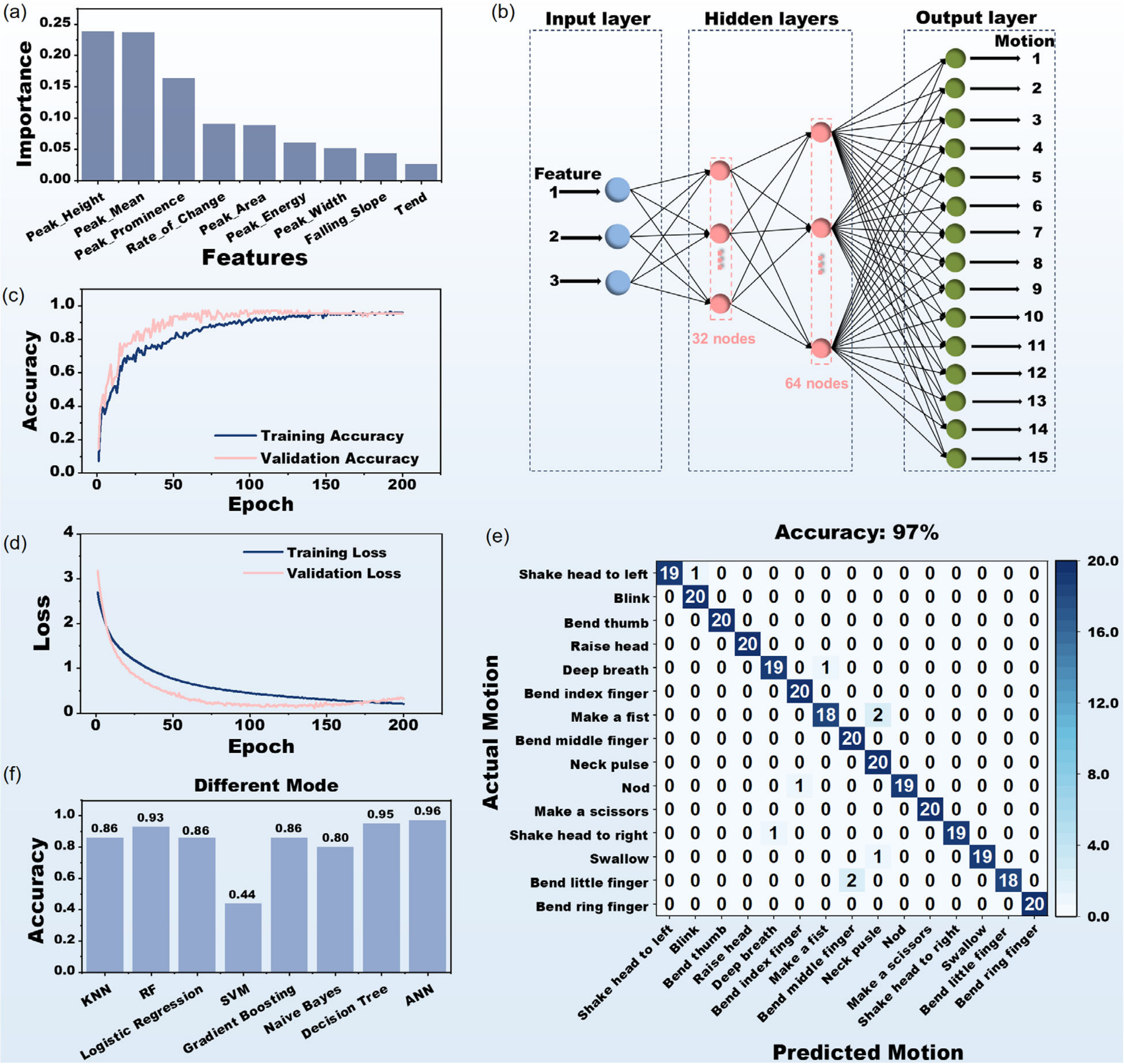

	Shake head to left	Blink	Bend thumb	Raise head	Deep breath	Bend index finger	Make a fist	Bend middle finger	Neck pusle	Nod	Make a scissors	Shake head to right	Swallow	Bend little finger	Bend ring finger
Shake head to left	19	1	0	0	0	0	0	0	0	0	0	0	0	0	0
Blink	0	20	0	0	0	0	0	0	0	0	0	0	0	0	0
Bend thumb	0	0	20	0	0	0	0	0	0	0	0	0	0	0	0
Raise head	0	0	0	20	0	0	0	0	0	0	0	0	0	0	0
Deep breath	0	0	0	0	19	0	1	0	0	0	0	0	0	0	0
Bend index finger	0	0	0	0	0	20	0	0	0	0	0	0	0	0	0
Make a fist	0	0	0	0	0	0	18	0	2	0	0	0	0	0	0
Bend middle finger	0	0	0	0	0	0	0	20	0	0	0	0	0	0	0
Neck pulse	0	0	0	0	0	0	0	0	20	0	0	0	0	0	0
Nod	0	0	0	0	0	1	0	0	0	19	0	0	0	0	0
Make a scissors	0	0	0	0	0	0	0	0	0	0	20	0	0	0	0
Shake head to right	0	0	0	0	1	0	0	0	0	0	0	19	0	0	0
Swallow	0	0	0	0	0	0	0	0	1	0	0	0	19	0	0
Bend little finger	0	0	0	0	0	0	0	2	0	0	0	0	0	18	0
Bend ring finger	0	0	0	0	0	0	0	0	0	0	0	0	0	0	20

Figure 6. Advanced recognition of human motions and physiological signals. a) Feature importance ranking of dynamic power data using Random Forest analysis. b) The topological architecture of a two-layer ANN (32→64 neurons) for sequential feature extraction. c) Training/validation accuracy progression over 200 epochs. d) Training/validation loss evolution over 200 epochs. e) Confusion matrix for the classification of 15 human motions and physiological activities. f) Prediction accuracy comparison of seven machine learning algorithms (KNN, RF, logistic regression, SVM, gradient boosting, Naïve Bayes, and decision tree).

solution highlights the plug-and-play functionality for expanding wearable application scenarios. A machine learning algorithm with 2D ANN-based SFE efficiently processes 15 human signals across diverse activities, achieving 97% classification accuracy for new subjects. Additionally, the versatility of the developed wearable integrated photonic sensing solution is evident as it provides comprehensive data that allows the feature extractor to adapt to new subjects. This adaptability is crucial for ongoing human health evaluation and facilitates continuous monitoring in everyday life scenarios, underscoring the platform's potential applications in real-world health management and diagnostic processes.

Supporting Information

Supporting Information is available from the Wiley Online Library or from the author.

Acknowledgements

Y.W. and K.B. contributed equally to this work. The team acknowledges support from the National Natural Science Foundation of China (62175202, 12104375), "Pioneer" and "Leading Goose" R&D Program of Zhejiang Province (2024SDXHDX0005), Key R&D Program of Zhejiang Province (2024C03150), Special Support Plan for Photoelectric Chips Research at Westlake University (10300000H062401/001), Key Project of

Westlake Institute for Optoelectronics (2023GD003/110500Y0022303). The authors would like to acknowledge the Westlake Center for Micro/Nano Fabrication and Instrumentation and ZJU Micro-Nano Fabrication Center at Zhejiang University for their facility support. Furthermore, the authors thank Mr. Xi Mu for deposition for E-beam evaporation and thank Xue Liu, Chen Ming, and Huiqin Wu for their contributions to EBL device fabrication. They also express appreciation to Yuxiang Zeng for her assistance in transmission spectrum characterization, Xinyu Qiao for his help in GSSe film fabrication, and Chaofeng Liu and Shuhua Wang for her advice in this work.

Conflict of Interest

The authors declare no conflict of interest.

Ethical Statement

This study involving human participants and the collection of wearable sensor-based motion data was reviewed and approved by the Ethics Committee of Westlake University (Approval Number: 20250303LL001). All participants provided written informed consent prior to their involvement in the study. The experimental procedures were non-invasive, involving only the attachment of wearable sensors to the body surface to acquire motion and physiological activity data. The study was conducted in accordance with the ethical principles of the Declaration of Helsinki and adhered to all relevant institutional and national guidelines for human subject research.

Data Availability Statement

The data that support the findings of this study are available from the corresponding author upon reasonable request.

Keywords

flexible sensor, full-packaged solution, machine learning algorithms, necklace-shaped microring resonator, wearable sensing

Received: April 15, 2025
Revised: June 17, 2025
Published online:

---

[1] Y. Luo, M. R. Abidian, J.-H. Ahn, D. Akinwande, A. M. Andrews, M. Antonietti, Z. Bao, M. Berggren, C. A. Berkey, C. J. Bettinger, J. Chen, P. Chen, W. Cheng, X. Cheng, S.-J. Choi, A. Chortos, C. Dagdeviren, R. H. Dauskardt, C.-a. Di, M. D. Dickey, X. Duan, A. Facchetti, Z. Fan, Y. Fang, J. Feng, X. Feng, H. Gao, W. Gao, X. Gong, C. F. Guo, et al., *ACS Nano* **2023**, *17*, 5211.

[2] Y. Khan, A. E. Ostfeld, C. M. Lochner, A. Pierre, A. C. Arias, *Adv. Mater.* **2016**, *28*, 4373.

[3] Z. Sun, M. Zhu, X. Shan, C. Lee, *Nat. Commun.* **2022**, *13*, 5224.

[4] J. Wang, Y. Zhu, Z. Wu, Y. Zhang, J. Lin, T. Chen, H. Liu, F. Wang, L. Sun, *Microsyst. Nanoeng.* **2022**, *8*, 16.

[5] Y. Lee, H. Rhee, G. Kim, W. H. Cheong, D. H. Kim, H. Song, S. N. Kay, J. Lee, K. M. Kim, *Nat. Commun.* **2025**, *16*, 4312.

[6] X. Wang, Y. Deng, X. Chen, P. Jiang, Y. K. Cheung, H. Yu, *Microsyst. Nanoeng.* **2021**, *7*, 99.

[7] Y. Shi, H. Li, L. Yang, Y. Wang, Z. Sun, C. Zhang, X. Fu, Y. Niu, C. Han, F. Xie, *Small Methods* **2024**, https://doi.org/10.1002/smtd.202401189.

[8] J. Li, H. Jia, J. Zhou, X. Huang, L. Xu, S. Jia, Z. Gao, K. Yao, D. Li, B. Zhang, Y. Liu, Y. Huang, Y. Hu, G. Zhao, Z. Xu, J. Li, C. K. Yiu, Y. Gao, M. Wu, Y. Jiao, Q. Zhang, X. Tai, R. H. Chan, Y. Zhang, X. Ma, X. Yu, *Nat. Commun.* **2023**, *14*, 5009.

[9] T. Saha, R. Del Caño, K. Mahato, E. De la Paz, C. Chen, S. Ding, L. Yin, J. Wang, *Chem. Rev.* **2023**, *123*, 7854.

[10] H. Song, H. Shin, H. Seo, W. Park, B. J. Joo, J. Kim, J. Kim, H. K. Kim, J. Kim, J.-U. Park, *Adv. Sci.* **2022**, *9*, 2203597.

[11] M. Wang, Y. Yang, J. Min, Y. Song, J. Tu, D. Mukasa, C. Ye, C. Xu, N. Heflin, J. S. McCune, T. K. Hsiai, Z. Li, W. Gao, *Nat. Biomed. Eng.* **2022**, *6*, 1225.

[12] H. Y. Y. Nyein, M. Bariya, B. Tran, C. H. Ahn, B. J. Brown, W. Ji, N. Davis, A. Javey, *Nat. Commun.* **2021**, *12*, 1823.

[13] R. Zhao, Y. He, Y. He, Z. Li, M. Chen, N. Zhou, G. Tao, C. Hou, *ACS Appl. Mater. Interfaces* **2023**, *15*, 16063.

[14] M. Han, H. Wang, Y. Yang, C. Liang, W. Bai, Z. Yan, H. Li, Y. Xue, X. Wang, B. Akar, H. Zhao, H. Luan, J. Lim, I. Kandela, G. A. Ameer, Y. Zhang, Y. Huang, J. A. Rogers, *Nat. Electron.* **2019**, *2*, 26.

[15] P. Zhu, Y. Wang, Y. Wang, H. Mao, Q. Zhang, Y. Deng, *Adv. Energy Mater.* **2020**, *10*, 2001945.

[16] D. Lu, T. Liu, X. Meng, B. Luo, J. Yuan, Y. Liu, S. Zhang, C. Cai, C. Gao, J. Wang, S. Wang, S. Nie, *Adv. Mater.* **2023**, *35*, 2209117.

[17] S. Wang, X. Wang, Q. Wang, S. Ma, J. Xiao, H. Liu, J. Pan, Z. Zhang, L. Zhang, *Adv. Mater.* **2023**, *35*, 2304701.

[18] S. Wang, J. Xu, W. Wang, G.-J. N. Wang, R. Rastak, F. Molina-Lopez, J. W. Chung, S. Niu, V. R. Feig, J. Lopez, T. Lei, S.-K. Kwon, Y. Kim, A. M. Foudeh, A. Ehrlich, A. Gasperini, Y. Yun, B. Murmann, J. B. H. Tok, Z. Bao, *Nature* **2018**, *555*, 83.

[19] L. Liu, J. Han, L. Xu, J. Zhou, C. Zhao, S. Ding, H. Shi, M. Xiao, L. Ding, Z. Ma, C. Jin, Z. Zhang, L.-M. Peng, *Science* **2020**, *368*, 850.

[20] M. Kaisti, T. Panula, J. Leppanen, R. Punkkinen, M. Jafari Tadi, T. Vasankari, S. Jaakkola, T. Kiviniemi, J. Airaksinen, P. Kostiainen, U. Meriheina, T. Koivisto, M. Pankaala, *NPJ Digital Medicine* **2019**, *2*, 39.

[21] F. Shi, N. Bamiedakis, P. P. Vasil'ev, R. V. Penty, I. H. White, D. Chu, *J. Lightwave Technol.* **2018**, *36*, 2685.

[22] S. Geiger, J. Michon, S. Liu, J. Qin, J. Ni, J. Hu, T. Gu, N. Lu, *ACS Photonics* **2020**, *7*, 2618.

[23] D. Hui, H. Alqattan, S. Zhang, V. Pervak, E. Chowdhury, M. T. Hassan, *Sci. Adv.* **2023**, *9*, adf1015.

[24] Q. Yu, Y. N. Zhang, L. Jiang, L. Li, X. Li, J. Zhao, *Small Methods* **2025**, *9*, 2401368.

[25] J. Shin, Z. Liu, W. Bai, Y. Liu, Y. Yan, Y. Xue, I. Kandela, M. Pezhouh, M. R. MacEwan, Y. Huang, W. Z. Ray, W. Zhou, J. A. Rogers, *Sci. Adv.* **2019**, *5*, aaw1899.

[26] N. Yao, X. Wang, S. Ma, X. Song, S. Wang, Z. Shi, J. Pan, S. Wang, J. Xiao, H. Liu, L. Yu, Y. Tang, Z. Zhang, X. Li, W. Fang, L. Zhang, L. Tong, *Photonics Res.* **2022**, *10*, 2040.

[27] W. Yu, N. Yao, J. Pan, W. Fang, X. Li, L. Tong, L. Zhang, *Opto-Electronic Advances* **2022**, *5*, 210101.

[28] H. Bai, S. Li, J. Barreiros, Y. Tu, C. R. Pollock, R. F. Shepherd, *Science* **2020**, *370*, 848.

[29] Z. Zhang, Y. Kang, N. Yao, J. Pan, W. Yu, Y. Tang, Y. Xu, L. Wang, L. Zhang, L. Tong, *Adv. Fiber Mater.* **2021**, *3*, 359.

[30] J. h. Li, J. h. Chen, F. Xu, *Adv. Mater. Technol.* **2018**, *3*, 1800296.

[31] L. Zhang, J. Pan, Z. Zhang, H. Wu, N. Yao, D. Cai, Y. Xu, J. Zhang, G. Sun, L. Wang, W. Geng, W. Jin, W. Fang, D. Di, L. Tong, *Opto-Electronic Advances* **2020**, *3*, 19002201.

[32] J. Pan, Q. Wang, S. Gao, Z. Zhang, Y. Xie, L. Yu, L. Zhang, *Opto-Electronic Advances* **2023**, *6*, 230076.

[33] G. Zhao, T. Wu, R. Wang, Z. Li, Q. Yang, L. Wang, H. Zhou, B. Jin, H. Liu, Y. Fang, D. Wang, F. Xu, *Sci. Adv.* **2023**, *9*, adj5407.

[34] J. Guo, X. Liu, N. Jiang, A. K. Yetisen, H. Yuk, C. Yang, A. Khademhosseini, X. Zhao, S.-H. Yun, *Adv. Mater.* **2016**, *28*, 10244.

[35] A. Leal-Junior, L. Avellar, V. Biazi, M. S. Soares, A. Frizera, C. Marques, *Opto-Electronic Advances* **2022**, *5*, 210098.
[36] J. Guo, M. Niu, C. Yang, *Optica* **2017**, *4*, 1285.
[37] A. Leber, B. Cholst, J. Sandt, N. Vogel, M. Kolle, *Adv. Funct. Mater.* **2019**, *29*, 1802629.
[38] X. Wang, H. Zhou, M. Chen, Y. He, Z. Zhang, J. Gan, Z. Yang, *Advanced Intelligent Systems* **2023**, *5*, 2200344.
[39] D. U. Kim, Y. J. Park, D. Y. Kim, Y. Jeong, M. G. Lim, M. S. Hong, M. J. Her, Y. Rah, D. J. Choi, S. Han, K. Yu, *Nat. Photonics* **2023**, *17*, 1089.
[40] H. Li, X. Li, Y. Yang, F. Xie, M. Han, Z. Lin, Y. Wang, J. Zhang, S. Zhang, C. Zhang, L. Cao, E. Li, *Optica* **2025**, *12*, 190.
[41] Z. Chen, Y. Shi, M. Wei, Y. Luo, H. Ma, R. Tang, Y. Weng, H. Dai, C. Zhong, C. Sun, L. Wang, K. Si, W. Gong, H. Lin, L. Li, *Adv. Opt. Mater.* **2023**, *11*, 2202824.
[42] R. Tang, C. Sun, K. Bao, Z. Chen, Z. Ju, M. Wei, Y. Wu, J. Wu, K. Xu, H. Lin, L. Li, *Laser Photonics Rev.* **2024**, *18*, 2300828.
[43] D. Kohler, G. Schindler, L. Hahn, J. Milvich, A. Hofmann, K. Länge, W. Freude, C. Koos, *Light: Sci. Applications* **2021**, *10*, 64.
[44] L. Li, H. Lin, Y. Huang, R.-J. Shiue, A. Yadav, J. Li, J. Michon, D. Englund, K. Richardson, T. Gu, J. Hu, *Optica* **2018**, *5*, 44.
[45] H. Schlicke, R. Maletz, C. Dornack, A. Fery, *Small* **2024**, *20*, 2403502.
[46] C. Zhang, H. Dong, C. Zhang, Y. Fan, J. Yao, Y. S. Zhao, *Sci. Adv.* **2021**, *7*, abh3530.
[47] H. Luan, Q. Zhang, T.-L. Liu, X. Wang, S. Zhao, H. Wang, S. Yao, Y. Xue, J. W. Kwak, W. Bai, Y. Xu, M. Han, K. Li, Z. Li, X. Ni, J. Ye, D. Choi, Q. Yang, J.-H. Kim, S. Li, S. Chen, C. Wu, D. Lu, J.-K. Chang, Z. Xie, Y. Huang, J. A. Rogers, *Sci. Adv.* **2021**, *7*, abj3686.
[48] J. Pan, Q. Li, Y. Feng, R. Zhong, Z. Fu, S. Yang, W. Sun, B. Zhang, Q. Sui, J. Chen, Y. Shen, Z. Li, *Nat. Commun.* **2023**, *14*, 3250.
[49] L. Fan, L. T. Varghese, Y. Xuan, J. Wang, B. Niu, M. Qi, *Opt. Express* **2012**, *20*, 20564.
[50] L. Li, H. Lin, S. Qiao, Y. Z. Huang, J. Y. Li, J. Michon, T. Gu, C. Alosno-Ramos, L. Vivien, A. Yadav, K. Richardson, N. Lu, J. Hu, *Light: Sci. Applications* **2018**, *7*, 17138.
[51] L. Li, H. Lin, S. Qiao, Y. Zou, S. Danto, K. Richardson, J. D. Musgraves, N. Lu, J. Hu, *Nat. Photonics* **2014**, *8*, 643.
[52] Y. Luo, C. Sun, M. Wei, H. Ma, Y. Wu, Z. Chen, H. Dai, J. Jian, B. Sun, C. Zhong, J. Li, K. A. Richardson, H. Lin, L. Li, *Nano Lett.* **2023**, *23*, 8898.
[53] R. Wei, H. Li, Z. Chen, Q. Hua, G. Shen, K. Jiang, *npj Flexible Electron.* **2024**, *8*, 83.
[54] L. Zhang, L. Jie, M. Zhang, Y. Wang, Y. Xie, Y. Shi, D. Dai, *Photonics Res.* **2020**, *8*, 684.
[55] F. P. Payne, J. P. R. Lacey, *Optical and Quantum Electronics* **1994**, *26*, 977.
[56] Z. Zhou, K. Chen, X. Li, S. Zhang, Y. Wu, Y. Zhou, K. Meng, C. Sun, Q. He, W. Fan, E. Fan, Z. Lin, X. Tan, W. Deng, J. Yang, J. Chen, *Nat. Electron.* **2020**, *3*, 571.
[57] J. Park, D.-h. Kang, H. Chae, S. K. Ghosh, C. Jeong, Y. Park, S. Cho, Y. Lee, J. Kim, Y. Ko, J. J. Kim, H. Ko, *Sci. Adv.* **2022**, *8*, abj9220.
[58] Z. Shen, Z. Zhang, N. Zhang, J. Li, P. Zhou, F. Hu, Y. Rong, B. Lu, G. Gu, *Adv. Mater.* **2022**, *34*, 2203650.
[59] F. Wen, Z. Zhang, T. He, C. Lee, *Nat. Commun.* **2021**, *12*, 5378.
[60] Y. Gao, H. Ota, E. W. Schaler, K. Chen, A. Zhao, W. Gao, H. M. Fahad, Y. Leng, A. Zheng, F. Xiong, C. Zhang, L.-C. Tai, P. Zhao, R. S. Fearing, A. Javey, *Adv. Mater.* **2017**, *29*, 1701985.